Lattice dynamics and structural phase transitions in $RbAlF_4$: group theory, inelastic neutron scattering results and the calculation of the phonon spectrum

1989 J. Phys.: Condens. Matter 1 4553

(http://iopscience.iop.org/0953-8984/1/28/007)

J. Phys.: Condens. Matter 1 (1989) 4553–4583. Printed in the UK

Lattice dynamics and structural phase transitions in $RbAlF_4$: group theory, inelastic neutron scattering results and the calculation of the phonon spectrum

A Bulou†, M Rousseau†, J Nouet† and B Hennion‡

† Laboratoire de Physique de l'Etat Condensé, CNRS No 807, Faculté des Sciences, Université du Maine, 72017 Le Mans Cédex, France

‡ Laboratoire Léon Brillouin, CNRS CEA Laboratory, CENS 91191, Gif-sur-Yvette Cédex, France

Received 4 October 1988, in final form 9 December 1988

Abstract. The low-frequency phonon spectrum of $RbAlF_4$ is investigated by inelastic neutron scattering at 400 °C. The two structural phase transitions at $T_{c1} = 280$ °C and at $T_{c2} = 9$ °C are shown to arise from the condensation of the zone boundary M_3 and X_3 soft modes, respectively, and they are preceded by the appearance of a central component. The symmetry properties of the vibrations in the ideal high-temperature phase are calculated and the compatibility relations of the symmetries between high- and low-temperature phases are given. A rigid ion model involving ten parameters is proposed to describe the phonon spectrum. Seventeen experimental data are used for the refinement; the discrepancy between experimental and calculated values is less than 10%. The main features of the spectrum are discussed, the Raman scattering anomalies are explained, and an attribution of infrared active modes is proposed. The Al–F short-range interaction parameters are given for the first time and the interionic distance dependence of the fluorine–fluorine short-range interaction parameters is deduced.

1. Introduction

A large number of AMF_4 compounds ($A = K^+, Rb^+, Tl^+, \ldots$ and $M = Al^{3+}, Fe^{3+}, Ti^{3+}, In^{3+} \ldots$) present a layered structure derived from the ideal so-called $TlAlF_4$-type structure (figure 1(*a*)) (Brosset 1937). It is made of MF_6 octahedra (figure 1(*b*)) linked together in a two-dimensional area (through 'equatorial fluorine' labelled F_{eq}) and disconnected along the third direction (axial fluorine labelled F_{ax}); such materials can be considered as layered perovskites. The two-dimensional properties also are evidenced macroscopically: these materials are easily cleaved and they look like micas; they have even been proposed to replace natural micas (Mockrin and Kowalski 1963). The interest in AMF_4 materials comes from the occurrence of a wide variety of structural phase transitions (SPTs). Peculiarly in case of tetrafluoroaluminates $AAlF_4$, the following transitions are observed: displacive SPTs by AlF_6 octahedra rotations in $RbAlF_4$ (Bulou and Nouet 1982) and $TlAlF_4$ (Bulou and Nouet 1987) as occur in fluoroperovskites; shear SPTs characteristic of the layered arrangement in $KalF_4$ (Launay *et al* 1985) similar to the martensitic transformations of metallic alloys; order–disorder SPTs in NH_4AlF_4

0953-8984/89/284553 + 31 $02.50

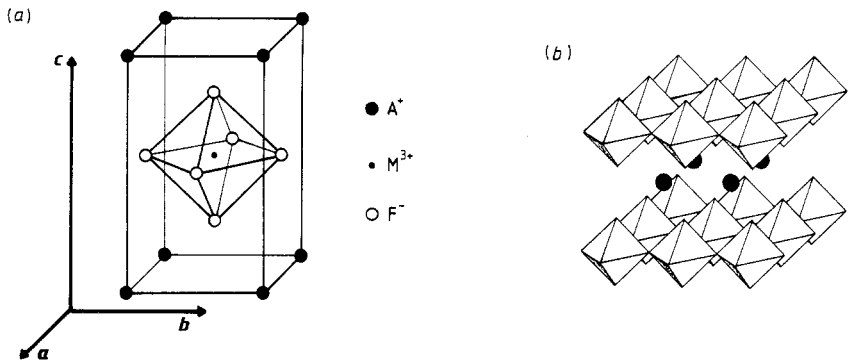

Figure 1. (*a*) The 'ideal' or 'aristotype' $TlAlF_4$ structure. A fluorine ion is called axial if it belongs to one octahedron (F_{ax}) and equatorial if it belongs to two octahedra (F_{eq}). (*b*) The clearly layered structure of AMF_4 compounds.

(Bulou *et al* 1982) where the two-dimensional ordering of the NH_4 network appears over a large temperature range above the transition (Dagorn *et al* 1985). It is the existence of these SPTs together with the quasi-two-dimensional properties that first stimulated the study of these materials.

With regard to such different behaviours it appeared interesting to investigate the lattice dynamics properties of these materials. A number of investigations have been performed by ultrasonics (Launay *et al* 1983). Raman scattering (Bulou *et al* 1983) and x-ray diffuse scattering (Gibaud *et al* 1987). However the information is always partial and complete analysis of the data together with comparison of the different behaviours cannot be done without a complete knowledge of the phonon spectrum of this structural arrangement. $RbAlF_4$ has been chosen for this study for the following reasons.

(i) At high temperature it exhibits the aristotype structure (highest symmetry structure).

(ii) It undergoes two structural phase transitions which can be described in terms of rotations of rigid AlF_6 octahedra. The sequence of structures is summarised in table 1. The two SPTs have been shown to be mainly displacive, they arise from condensation of soft modes setting at two different symmetry points of the Brillouin zone. Due to this feature it is possible to determine the frequency of a large number of zone boundary modes via zone centre spectrometry such as Raman scattering (Bulou *et al* 1983) or infrared absorption.

(iii) It contains only diamagnetic ions which avoids any perturbation by magnetic ordering.

(iv) All the ions have a somewhat small polarisability and it can be expected to describe the phonon spectrum with simple lattice dynamics models such as a rigid ion model.

Moreover the two transitions in $RbAlF_4$ are of special interest in themselves since the three-dimensional ordering probably proceeds from two different mechanisms. (1) At the T_{c1} SPTs the two-dimensional octahedral tilts can be explained by the AlF_6 octahedra rigidity like in fluoroperovskites, the correlation along the third direction remaining unexplained. (2) At the T_{c2} SPTs no two-dimensional correlation can be so easily invoked since the AlF_6 octahedra are disconnected along the tetragonal axis.

Table 1. Main features of structural phase transitions in $RbAlF_4$. φ_1, φ_2, φ_3 represent the octahedra rotations around |100|, |010| and |001| axes, respectively.

	Phase III	$T_{c2} \simeq 9$ °C	Phase II	$T_{c1} = 280$ °C	Phase I ($T_f \simeq 580$ °C)
Space group	Pmmn D_{2h}^{13}		P4/mbm D_{4h}^{5}		P4/mmm D_{4h}^{1}
Cell	$\boldsymbol{a}_{III} = 2\boldsymbol{a}$		$\boldsymbol{a}_{II} = \boldsymbol{a} + \boldsymbol{b}$		$\boldsymbol{a}$
parameters	$\boldsymbol{b}_{III} = 2\boldsymbol{b}$		$\boldsymbol{b}_{II} = -\boldsymbol{a} + \boldsymbol{b}$		$\boldsymbol{b}$
	$\boldsymbol{c}_{III} = \boldsymbol{c}$		$\boldsymbol{c}_{II} = \boldsymbol{c}$		$\boldsymbol{c}$
Tilt system	$a_p^+ b_p^+ c^+$		$a^0 a^0 c^+$		$a^0 a^0 c^0$
Order		Second		First	
Latent heat (J mol^{-1})		0		180	
Order parameter		$\varphi = [\varphi_1 \cdot \varphi_2]$		$\varphi = \varphi_3$	
Ferroicity		Improper ferroelastic		Non-ferroic	

Table 2. Ionic coordinates of the six ions belonging to the unit cell of $RbAlF_4$ in the aristotype phase.

	Reduced coordinates		
Atom	x	y	z
Al	0	0	0
A	1/2	1/2	1/2
F_{eq_1}	1/2	0	0
F_{eq_2}	0	1/2	0
F_{ax_1}	0	0	z
F_{ax_2}	0	0	$-z$

Investigations of the lattice dynamics properties would bring some light about the origin of these correlations.

To conclude, the purpose of this paper is to report on the lattice dynamics properties of the 'ideal' $TlAlF_4$ structure (aristotype structure) and it is applied to $RbAlF_4$, one of the few compounds that exhibits a phase with this ideal structure. In a first step (§ 2) the symmetries of the vibrations of this structural arrangement in the aristotype phase are determined. The phonon spectrum is experimentally investigated by inelastic neutron scattering in the aristotype phase and the soft modes responsible for the transition are studied against temperature (§ 3). It is followed by the calculation of the phonon spectrum with a rigid ion model and the discussion of the results (§ 4).

2. Group theory analysis of the normal modes

2.1. *Normal modes symmetry, symmetry adapted eigenvectors and compatibility conditions*

The aristotype structure of the layered AMF_4 belongs to the P4/mmm space group with one formula unit per unit cell, i.e., with six ions per cell. The conventions for ions labelling are reported in table 2. The symmetries of the normal vibration modes are determined by the method given by Maradudin and Vosko (1968) and by Warren (1968). The Brillouin zone of the tetragonal primitive cell of the aristotype structure is represented in figure 2.

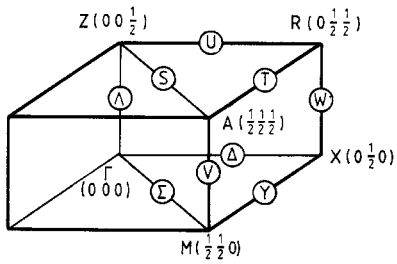

Figure 2. Representation of the high-symmetry points and lines of the tetragonal primitive Brillouin zone (⅛ of zone).

Table 3. Reduction into irreducible representations of the mechanical representation $T(q)$ and symmetry-adapted eigenvectors $E(qs)$. The coefficients $\alpha, \beta, \gamma, \delta, \varepsilon$ and φ are real and $i = \sqrt{-1}$. In all cases $\rho = \exp i\pi\mu$ where μ stands for the reduced components of the wavevector q.

(*a*)

$E(q:s)$		Representation C_s	Γ_1	Γ_4	Γ_8	Γ_9		Γ_{10}		Σ_1	Σ_2	Σ_3	Σ_4
			1	4	1	1		5		6	2	5	5
Al	x							α	α	α		α	
	y							$-\alpha$	α	α		$-\alpha$	
	z			α									α
A	x							β	β	$\rho^2\beta$		$\rho^2\beta$	
	y							$-\beta$	β	$\rho^2\beta$		$-\rho^2\beta$	
	z			β									$\rho^2\beta$
F_{eq_1}	x							γ	γ	$\rho\gamma$		$\rho\gamma$	
	y							δ	$-\delta$	$\rho\delta$		$\rho\delta$	
	z			γ	$1/\sqrt{2}$						$\rho\alpha$		$\rho\gamma$
F_{eq_2}	x							$-\delta$	$-\delta$	$\rho\delta$		$-\rho\delta$	
	y							$-\gamma$	γ	$\rho\gamma$		$-\rho\gamma$	
	z			γ	$-1/\sqrt{2}$						$-\rho\alpha$		$\rho\delta$
F_{ax_1}	x					$\frac{1}{2}$	$-\frac{1}{2}$	ε	ε	ε	$i\beta$	ε	$i\delta$
	y					$\frac{1}{2}$	$\frac{1}{2}$	$-\varepsilon$	ε	ε	$-i\beta$	$-\varepsilon$	$i\delta$
	z		$1/\sqrt{2}$	δ						$i\varphi$			ε
F_{ax_2}	x					$-\frac{1}{2}$	$\frac{1}{2}$	ε	ε	ε	$-i\beta$	ε	$-i\delta$
	y					$-\frac{1}{2}$	$-\frac{1}{2}$	$-\varepsilon$	ε	ε	$i\beta$	$-\varepsilon$	$-i\delta$
	z		$-1/\sqrt{2}$	δ						$-i\varphi$			ε

(*b*)

$E(q:s)$		Representation C_s	M_1	M_3	M_4	M_5	M_6	M_7	M_9		M_{10}	
			2	1	2	1	1	1	2		3	
Al	x										α	α
	y										$-\alpha$	α
	z				α							
A	x										β	$-\beta$
	y										$-\beta$	$-\beta$
	z						1					
F_{eq_1}	x		α			$1/\sqrt{2}$						
	y			$1/\sqrt{2}$				$1/\sqrt{2}$				
	z								α	$-\alpha$		
F_{eq_2}	x			$-1/\sqrt{2}$				$1/\sqrt{2}$				
	y		α			$-1/\sqrt{2}$						
	z								α	α		
F_{ax_1}	x								β	$-\beta$	$-\gamma$	γ
	y								β	β	γ	γ
	z		β		β							
F_{ax_2}	x								$-\beta$	β	γ	γ
	y								$-\beta$	$-\beta$	$-\gamma$	γ
	z		$-\beta$		β							

Table 3.—*continued*

(*c*)

Representation C_s / $E(q:s)$		X_1 3	X_3 3	X_4 3	X_5 1	X_6 3	X_7 2	X_8 3	Δ_1 6	Δ_2 1	Δ_3 6	Δ_4 5
Al	x			α								α
	y					α			α			
	z							α			α	
A	x						α					$\rho\beta$
	y		α						$\rho\beta$			
	z			α							$\rho\beta$	
F_{eq_1}	x			β								γ
	y					β			γ			
	z							β			γ	
F_{eq_2}	x						β					$\rho\delta$
	y		β						$\rho\delta$			
	z			β							$\rho\delta$	
F_{ax_1}	x			γ	$1/\sqrt{2}$					$1/\sqrt{2}$		ε
	y		γ			γ			ε		iε	
	z		γ					γ	iφ		φ	
F_{ax_2}	x			γ	$-1/\sqrt{2}$					$-1/\sqrt{2}$		ε
	y		$-\gamma$			γ			ε		$-$iε	
	z		$-\gamma$					γ	$-$iφ		φ	

(*d*)

Representation C_s / $E(q:s)$		Z_1 2	Z_4 3	Z_8 1	Z_9 2		Z_{10} 4		Λ_1 5	Λ_3 1	Λ_5 6	
Al	x						α	α			α	$-\alpha$
	y						$-\alpha$	α			α	α
	z		α						α			
A	x				α	$-\alpha$					$\rho\beta$	$-\rho\beta$
	y				α	α					$\rho\beta$	$\rho\beta$
	z	α							$\rho\beta$			
F_{eq_1}	x						β	β			γ	$-\gamma$
	y						γ	$-\gamma$			δ	δ
	z		β	$1/\sqrt{2}$					γ	$1/\sqrt{2}$		
F_{eq_2}	x						$-\gamma$	$-\gamma$			δ	$-\delta$
	y						$-\beta$	β			γ	γ
	z		β	$-1/\sqrt{2}$					γ	$-1/\sqrt{2}$		
F_{ax_1}	x				β	$-\beta$	δ	δ			$\varepsilon+$iφ	$-(\varepsilon+$i$\varphi)$
	y				β	β	$-\delta$	δ			$\varepsilon+$iφ	$(\varepsilon+$i$\varphi)$
	z	β	γ						$\delta+$iε			
F_{ax_2}	x				$-\beta$	β	δ	δ			$\varepsilon-$iφ	$-(\varepsilon-$i$\varphi)$
	y				$-\beta$	$-\beta$	$-\delta$	δ			$\varepsilon-$iφ	$(\varepsilon-$i$\varphi)$
	z	$-\beta$	γ						$\delta-$iε			

Table 3.—*continued*

(*e*)

Representation C_s / $E(q:s)$		A_1	A_3	A_4	A_5	A_7	A_9		A_{10}	
		2	1	2	1	2	3		2	
Al	x								α	α
	y								$-\alpha$	α
	z			α						
A	x						α	α		
	y						α	$-\alpha$		
	z					α				
F_{eq_1}	x	α			$1/\sqrt{2}$					
	y		$1/\sqrt{2}$			β				
	z						β	$-\beta$		
F_{eq_2}	x		$-1/\sqrt{2}$			β				
	y	α			$-1/\sqrt{2}$					
	z						β	β		
F_{ax_1}	x						γ	$-\gamma$	β	β
	y						γ	γ	$-\beta$	β
	z	β		β						
F_{ax_2}	x						$-\gamma$	γ	β	β
	y						$-\gamma$	$-\gamma$	$-\beta$	β
	z	$-\beta$		β						

(*f*)

Representation C_s / $E(q:s)$		R_1	R_2	R_3	R_4	R_5	R_6	R_7	R_8
		2	1	2	3	1	4	1	4
Al	x				α				
	y						α		
	z								α
A	x		1						
	y								β
	z						β		
F_{eq_1}	x				β				
	y						γ		
	z								γ
F_{eq_2}	x							1	
	y	α							
	z			α					
F_{ax_1}	x				γ	$1/\sqrt{2}$			
	y			β			δ		
	z	β							δ
F_{ax_2}	x				γ	$-1/\sqrt{2}$			
	y			$-\beta$			δ		
	z	$-\beta$							δ

Table 3.—*continued*

(*g*)

$E(q:s)$		Representation C_s	V_1 4	V_2 1	V_3 1	V_4 2	V_5 5		Y_1 6	Y_2 3	Y_3 4	Y_4 5
Al	x						α	$-\alpha$	α			
	y						α	α				α
	z		α								α	
A	x						$\rho\beta$	$\rho\beta$				$i\rho\beta$
	y						$\rho\beta$	$-\rho\beta$	$i\rho\beta$			
	z					$\rho\alpha$				$i\rho\alpha$		
F_{eq_1}	x		$i\beta$		$1/\sqrt{2}$				$\rho\gamma$			
	y			$1/\sqrt{2}$		$i\beta$						$\rho\gamma$
	z						$i\gamma$	$-i\gamma$			$\rho\beta$	
F_{eq_2}	x			$-1/\sqrt{2}$		$i\beta$						$i\delta$
	y		$i\beta$		$-1/\sqrt{2}$				$i\delta$			
	z						$i\gamma$	$i\gamma$		$i\beta$		
F_{ax_1}	x						$\delta + i\varepsilon$	$-(\delta + i\varepsilon)$	ε		$i\gamma$	
	y						$\delta + i\varepsilon$	$\delta + i\varepsilon$		$i\gamma$		ε
	z		$\gamma + i\delta$						$i\varphi$		δ	
F_{ax_2}	x						$\delta - i\varepsilon$	$-(\delta - i\varepsilon)$	ε		$-i\gamma$	
	y						$\delta - i\varepsilon$	$(\delta - i\varepsilon)$		$-i\gamma$		ε
	z		$\gamma - i\delta$						$-i\varphi$		δ	

(*h*)

$E(q:s)$		Representation C_s	W_1 6	W_2 2	W_3 6	W_4 4	U_1 6	U_2 2	U_3 6	U_4 4
Al	x					α				α
	y				α		α			
	z		α						α	
A	x			$i\rho\alpha$				$i\rho\alpha$		
	y		$i\rho\beta$						$i\rho\beta$	
	z				$i\rho\beta$		$i\rho\beta$			
F_{eq_1}	x					β				β
	y				γ		γ			
	z		γ						γ	
F_{eq_2}	x			$i\beta$						$\rho\gamma$
	y		$i\delta$				$\rho\delta$			
	z				$i\delta$				$\rho\delta$	
F_{ax_1}	x					$\gamma + i\delta$		$i\beta$		δ
	y				$\varepsilon + i\varphi$		ε		$i\varepsilon$	
	z		$\varepsilon + i\varphi$				$i\varphi$		φ	
F_{ax_2}	x					$\gamma - i\delta$		$-i\beta$		δ
	y				$\varepsilon - i\varphi$		ε		$-i\varepsilon$	
	z		$\varepsilon - i\varphi$				$-i\varphi$		φ	

Table 3.—*continued*

(*i*)

$E(q:s)$		Representation C_s	S_1 6	S_2 3	S_3 4	S_4 5	T_1 5	T_2 3	T_3 5	T_4 5
Al	x		α		α		α			
	y		α		$-\alpha$					α
	z					α			α	
A	x			$i\rho^2\alpha$		$i\rho^2\beta$	$\rho\alpha$			
	y			$-i\rho^2\alpha$		$i\rho^2\beta$			$\rho\beta$	
	z		$i\rho^2\beta$							$\rho\beta$
F_{eq_1}	x		$\rho\gamma$		$\rho\beta$		$\rho\beta$			
	y		$\rho\delta$		$\rho\gamma$					$\rho\gamma$
	z			$\rho\beta$		$\rho\gamma$			$\rho\gamma$	
F_{eq_2}	x		$\rho\delta$		$-\rho\gamma$					$i\delta$
	y		$\rho\gamma$		$-\rho\beta$		$i\gamma$			
	z			$-\rho\beta$		$\rho\gamma$		$i\beta$		
F_{ax_1}	x		ε	$i\gamma$	δ	$i\delta$	δ		$i\delta$	
	y		ε	$-i\gamma$	$-\delta$	$i\delta$		$i\gamma$		ε
	z		$i\varphi$			ε	$i\varepsilon$		ε	
F_{ax_2}	x		ε	$-i\gamma$	δ	$-i\delta$	δ		$-i\delta$	
	y		ε	$i\gamma$	$-\delta$	$-i\delta$		$-i\gamma$		ε
	z		$-i\varphi$			ε	$-i\varepsilon$		ε	

Following Maradudin and Vosko the symmetry properties of the normal modes of vibrations can be deduced from a matrix representation $\mathbf{T}(\boldsymbol{q})$ of the group of the wave vector $\boldsymbol{q}$ whose matrices $\mathbf{T}(\boldsymbol{q}; R)$ commute with the dynamical matrix (R is the point symmetry operator of group of the wavevector $\boldsymbol{q}$). This representation can be reduced into irreducible components:

$$\mathbf{T}(\boldsymbol{q}) = \sum_s C_s \tau^{(s)}(\boldsymbol{q})$$

where C_s represents the number of the vibrational modes which transform according to the $\tau^{(s)}(\boldsymbol{q})$ irreducible representation of the group of the wavevector $\boldsymbol{q}$. Tables 3 give the values of C_s for all the symmetry points and symmetry lines of the aristotype structure Brillouin zone. In this table P_s notation (respectively L_s) represents the irreducible representation $\tau^{(s)}(\boldsymbol{q})$ of Kovalev (1965) for the wavevector $\boldsymbol{q}$ corresponding to the P symmetry point (respectively L symmetry line). The representation $T(\boldsymbol{q})$ also makes it possible to calculate the projection operator matrix and to deduce the symmetry-adapted eigenvector $\boldsymbol{E}(\boldsymbol{q}, s\lambda)$, where λ represents the n components of an irreducible representation n-times degenerated. These symmetry adapted eigenvectors are given in tables 3 (when $C_s = 1$ they are just the normal mode coordinates).

In order to establish the connectivity of branches of the dispersion relation the compatibility conditions have been established, and are given in figure 3.

2.2. *Soft modes*

From the relations between the unit cell of the three phases (table 1) the correspondence

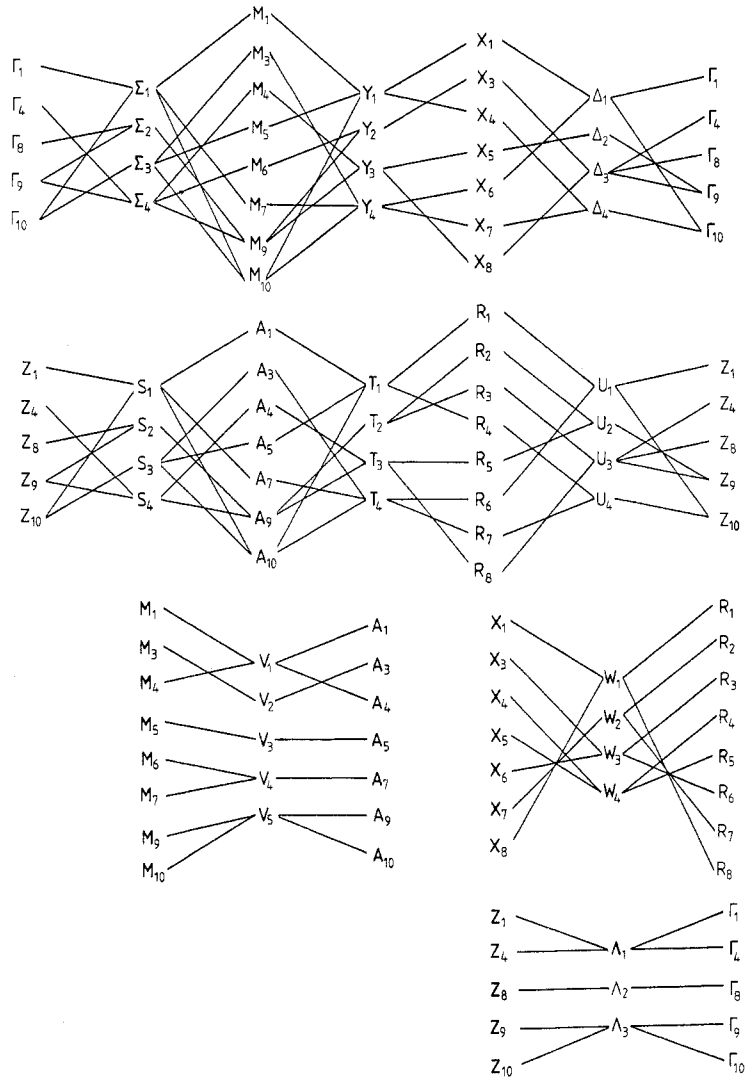

Figure 3. Point–line compatibilities of the vibrational mode symmetries.

between the reciprocal lattices can be deduced, as represented in figure 4. It is evident that the I–II transition can be attributed to condensation of a mode located at the M point of the Brillouin zone of the ideal phase. The transition arises from the AlF_6 octahedra tilts around the tetragonal axis, i.e., can be imputed to the condensation of the M_3 symmetry mode (table 3(*b*)). Similarly, figure 4 shows that the II–III transition can be imputed to the condensation of a mode located at the M_{II} point of phase II Brillouin zone (tetragonal primitive lattice like in phase I), i.e., at the X point of the Brillouin zone of phase I. The ionic displacements in phase III correspond to AlF_6 rotations around the [100] and [010] axes together with translations of rubidium along the [001] axis: such displacements correspond to one of the three X_3 symmetry modes with wavevector $\boldsymbol{q} = (0, \frac{1}{2}, 0)$. However, it must be noted that the star of the wavevector

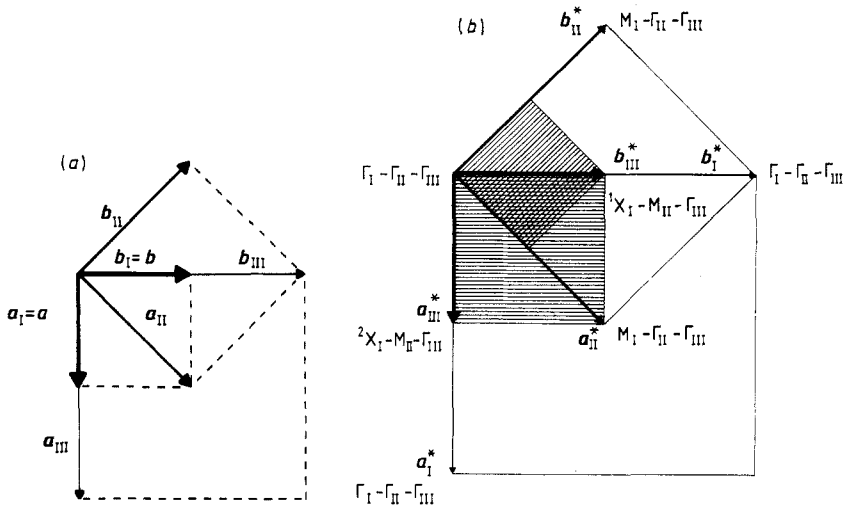

Figure 4. (*a*) Relationship between cell parameters in the (001) plane for the three phases of $RbAlF_4$. (*b*) Projection in the (001) plane of the reciprocal lattices of the three phases of $RbAlF_4$. The hatched squares represent $\frac{1}{4}$ of the Brillouin zone of phase I and II cells.

has two arms defined by $\boldsymbol{q}_1 = (0, \frac{1}{2}, 0)$ corresponding to the ^1X point and $\boldsymbol{q}_2 = (\frac{1}{2}, 0, 0)$ corresponding to the ^2X point. While in phase I these two wavevectors are not equivalent, in phase II they correspond to two M_{II} points equivalent at a reciprocal lattice vector. Then the $^1X_3$ and $^2X_3$ non-degenerated modes in phase I are twice degenerated in phase II.

2.3. Compatibility relations between the three phases

The determination of the symmetry of the modes at the Brillouin zone centre in the three phases is useful for spectroscopic studies. In the low-temperature phase however the number of irreducible representations is small and only limited information can be inferred from group theory.

In a case such as $RbAlF_4$ the modes can be classified not only according to their symmetry but also according to the phase in which they become active. The vibrational ionic displacements in the lower-temperature phase can be thought close to the ionic vibrations in the ideal phase where the amount of information given by group theory is more important. Moreover, except for the soft mode, it can be expected that the frequencies undergo very little variation. Thus it is useful to establish compatibility relations between the mode symmetries at zone centre in the three phases and the corresponding symmetries in the high-temperature phase (at the M and X point):

$$\begin{array}{ccccc} & & \Gamma(\mathrm{I}) \rightarrow \Gamma(\mathrm{II}) \leftarrow \mathrm{M(I)} & & \\ \Gamma(\mathrm{I}) & \searrow & & \swarrow & {}^1\mathrm{X(I)} \\ & & \Gamma(\mathrm{II}) \rightarrow \Gamma(\mathrm{III}) \leftarrow \mathrm{M(II)} & & \\ \mathrm{M(I)} & \nearrow & & \nwarrow & {}^2\mathrm{X(I)}. \end{array}$$

This is performed by the usual method consisting in the reduction of the irreducible representation of the point group of the wavevector of the ideal phase $G_0(\boldsymbol{q})$ into the irreducible representations of the point group of the wavevector $G_0'(\boldsymbol{q}')$ in the lower-symmetry phase. However in case of the relations X(I) → M(II) the group of the wavevector $G_0(\boldsymbol{q})$ is not a subgroup of $G_0(\boldsymbol{q})$ and it has been necessary to consider the representations of the space group itself.

The results are given in diagrammatic form in figure 5. It appears that the nine A_g modes in phase III that could not be distinguished according to group theory in this phase, can be classified into four different types according to their corresponding symmetries in the ideal phase. The atomic displacements are determined from tables 3.

It can be noted that the M_3 mode mentioned above gives rise in phase II to the totally symmetric A_{1g} mode: this is the criterion defining an order parameter for a second-order or a weakly first-order structural phase transition. The same applies to the $M_1 \oplus M_7$

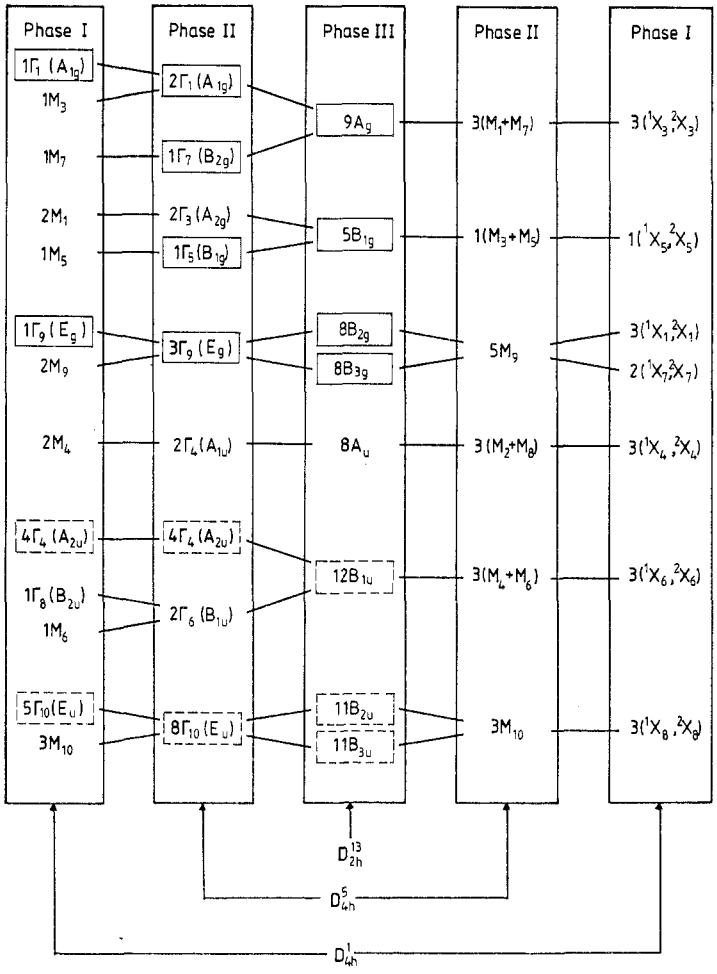

Figure 5. Compatibility relations diagram of the vibrational symmetries for the three phases of $RbAlF_4$. Modes surrounded by full and dashed lines are Raman and infrared-active modes, respectively.

symmetry mode at the second transition. Thus only the M_3 mode of phase I and $M_1 \oplus M_7$ mode of phase II can be chosen as order parameters for the T_{c1} and T_{c2} transitions respectively.

In figure 5 the modes surrounded by solid and dashed lines are Raman and infrared-active, respectively. Since the structural phase transitions arise from condensations at two different points of the Brillouin zone it is possible to obtain information on the phonon spectrum by zone centre spectroscopy in the low-temperature phases. This will be used in § 4.

3. Inelastic neutron scattering results

Inelastic neutron scattering studies of $RbAlF_4$ have been performed at 400 °C in order to determine the main features of the phonon spectrum in the aristotype structure. These results are followed by an analysis of the temperature behaviour in phases I and II of the M_3 and X_3 phonons responsible for the transitions.

3.1. Experimental details

The sample consists in a single crystal of about 1 cm^3 grown at the Laboratoire de Physique de l'Etat Condensé (Le Mans) by Bridgmann technique in a platinum-sealed crucible. The mosaic spread of the crystal is about 1°.

The experiments were performed on the 1T inelastic neutron scattering spectrometer of LLB (Saclay) with Ge(111) monochromator and pyrolytic graphite (002) analyser. Measurements were made at constant wavevector k_i in the range 4 $Å^{-1}$ to 2 $Å^{-1}$. A pyrolytic graphite filter was used for the study of the soft modes at $k_i = 2.662$ $Å^{-1}$ and $k_i = 2.0$ $Å^{-1}$. In the experiments the sample was set in a furnace and heated in a vacuum; the studies of the frequency of the soft X_3 mode were performed in a cryofurnace.

In investigations of the phonon spectrum of $RbAlF_4$ several modes appear to be particularly important in addition to the expected soft modes M_3 and X_3. These are the acoustic modes and the M_6, M_9 and X_7 symmetry modes for which analytical expressions of the frequencies can be obtained (see below). Four scattering planes $(h,h,0)$, $(0,k,l)$, (h,h,l) and $(h,3.5h,0)$ are then necessary to get this information. In order to select the best conditions for the study of each mode dynamical structure factors have been calculated using the rigid-ion model presented in § 4.

3.2. Low-frequency phonon spectrum of $RbAlF_4$

The low-frequency phonon spectrum of $RbAlF_4$ obtained at 400 °C is reported in figures 6 for the ΓMXΓ and ΓXRZΓ planes. The values represented by a point or a bar have been fitted taking into account the apparatus function. The general features of the spectrum are outlined below. However, it can be remarked the low frequency of the M_3 and X_3^1 phonons condense at T_{c1} and T_{c2}, respectively.

The constant Q scans collected at the M (0.5, 1.5, 0) and X (0, 0.5, 3) points of the ideal Brillouin zone at several temperatures are shown in figure 7. As expected, these modes soften when the transitions are approached. (However, it can be noted that below T_{c1}, although the soft M_3 mode frequency was known from Raman scattering studies, attempts to observe this mode by inelastic neutron scattering failed.) The M_3 mode is overdamped on a wide temperature range, and frequency determination is difficult. On

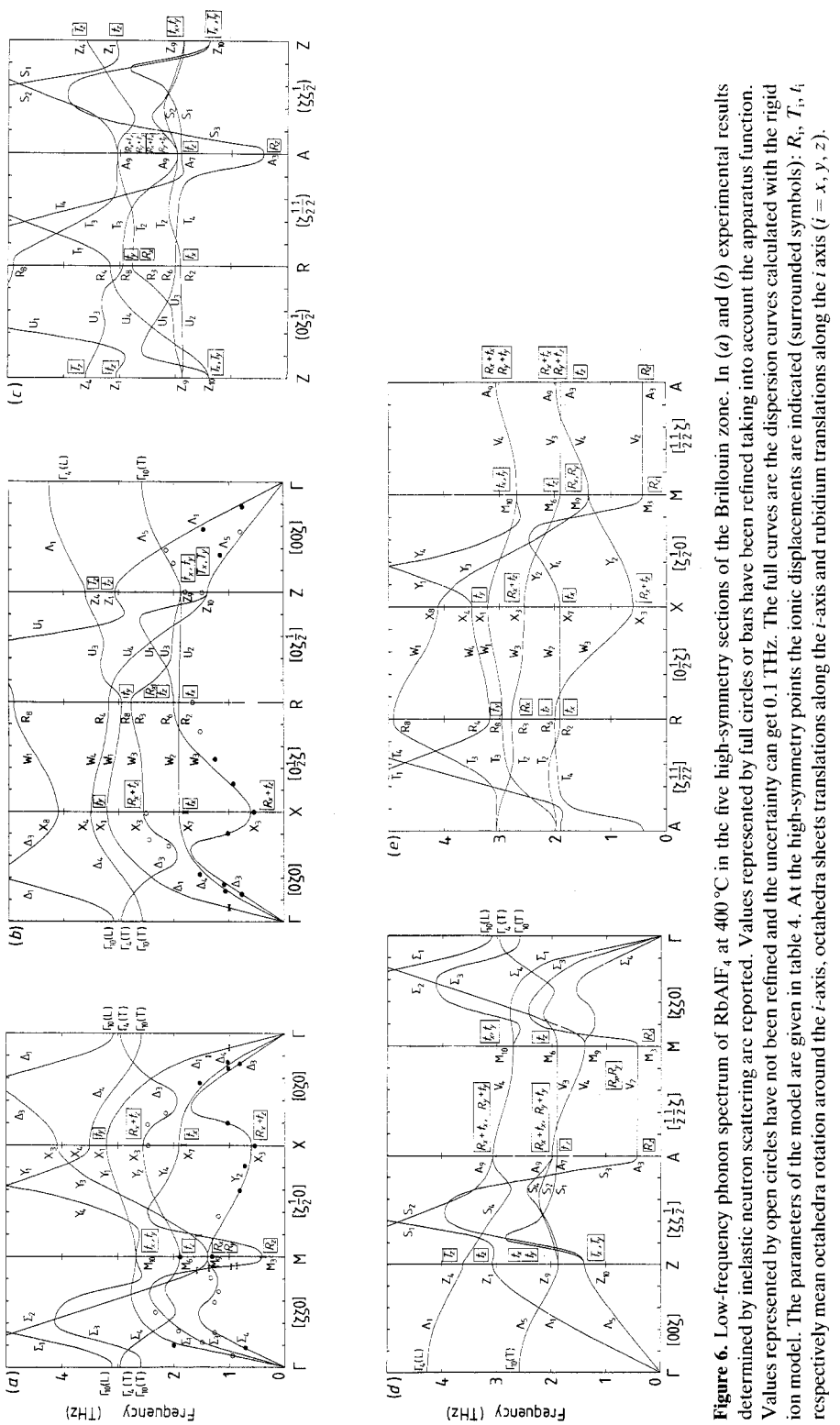

Figure 6. Low-frequency phonon spectrum of $RbAlF_4$ at 400 °C in the five high-symmetry sections of the Brillouin zone. In (*a*) and (*b*) experimental results determined by inelastic neutron scattering are reported. Values represented by full circles or bars have been refined taking into account the apparatus function. Values represented by open circles have not been refined and the uncertainty can get 0.1 THz. The full curves are the dispersion curves calculated with the rigid ion model. The parameters of the model are given in table 4. At the high-symmetry points the ionic displacements are indicated (surrounded symbols): R_i, T_i, t_i respectively mean octahedra rotation around the *i*-axis, octahedra sheets translations along the *i*-axis and rubidium translations along the *i* axis ($i = x, y, z$).

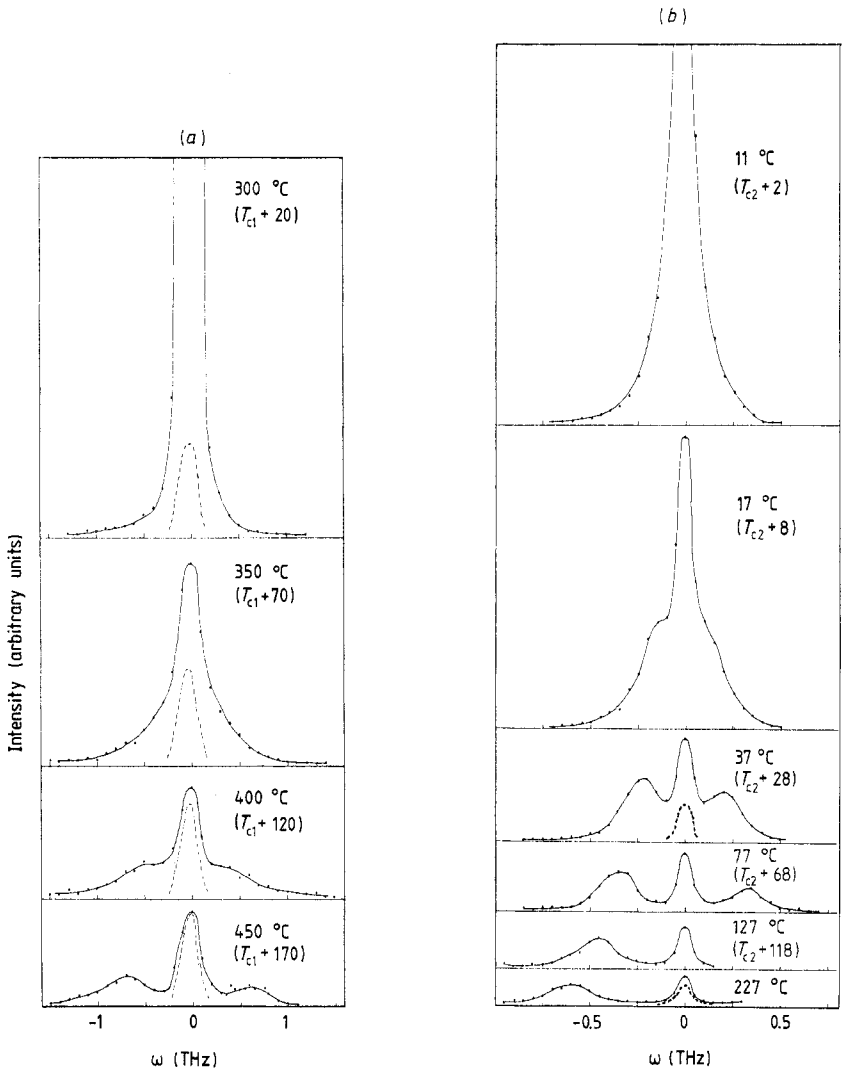

Figure 7. Scattered neutron spectra of $RbAlF_4$ at several temperatures (points) and incoherent elastic contribution measured with same transfer moment (dashed lines). Measurements have been performed with graphic filter. (*a*) soft M_3 phonon profile collected at $Q = (0.5, 1.5, 0)$ and incoherent elastic contribution measured at $Q = (0.79, 1.37, 0)$. (k_i = 2.662 Å^{-1}). (*b*) soft X_3^1 phonon profile collected at $Q = (0, 0.5, 3)$ and incoherent elastic contribution measured at $Q = (0, 0.8, 2.8)$. (k_i = 2.0 Å^{-1}).

the other hand, the temperature range where the X_3 mode is overdamped is much narrower; its frequency is plotted against temperature in figure 8. The frequency exhibits the classical behaviour for second-order phase transitions, i.e., $\omega^2 = \alpha(T - T_c)$ with T_c = 278 (4) K; a similar law used to describe the soft-mode behaviour below the transition, measured by Raman scattering, leads to T_c = 284 (2) K.

In addition, when the transitions are approached from above, zero-frequency components are observed and their intensities rapidly increase when temperature decreases.

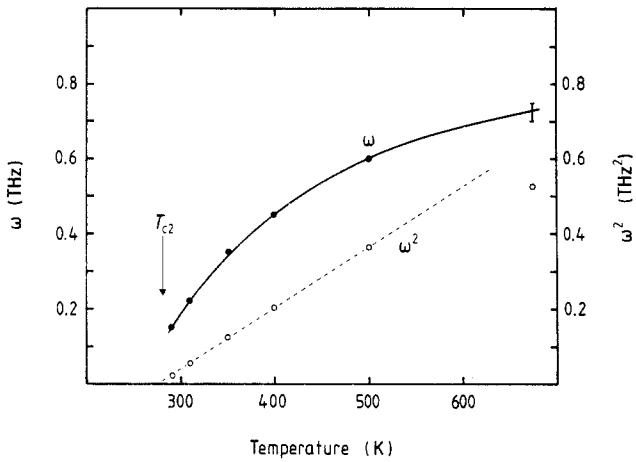

Figure 8. Temperature behaviour of the soft X_3^+ phonon frequency (full circles) and of the square of this frequency (open circles) for $RbAlF_4$.

This seems to be similar to the central peaks of perovskites (Shapiro *et al* 1972, Rousseau *et al* 1976). The incoherent elastic diffusion has been measured at the points (0.79, 1.37, 0) and (0, 0.8, 2.8) with the same transfer moments as the points (0.5, 1.5, 0) and (0, 0.5, 3), respectively. This contribution is also plotted in figure 7; it appears that the central components begin to grow about 100° above the transitions.

4. Calculation of the phonon spectrum

$RbAlF_4$, one of the layered AMF_4 compounds exhibiting the ideal higher-symmetry structure, can be considered as a reference. Knowledge of its phonon spectrum is useful in explaining its temperature behaviour and also the different behaviours of other AMF_4 compounds. With regard to the number of experimental data available on $RbAlF_4$ (ultrasonic velocities, Raman scattering frequencies, infrared frequencies and the above inelastic neutron scattering data) results of a lattice dynamical model can be checked. However, due to the complexity of the system the number of model parameters could be important which would preclude the prediction of the phonon spectrum of isomorphous materials. For this reason a description with a rigid-ion model involving a small number of parameters has been chosen.

4.1. Dynamical matrix parameters

For a wavevector $\boldsymbol{q}$ the phonons frequencies $\omega_j^2(\boldsymbol{q})$ and the corresponding ionic displacements are the eigenvalues and the eigenvectors of the so-called $3n \times 3n$ dynamical matrix $\mathbf{C}(\boldsymbol{q})$ with components:

$$\mathbf{C}_{\alpha\beta}(\kappa, \kappa'|\boldsymbol{q}) = \frac{1}{\sqrt{M_\kappa M_{\kappa'}}} \sum_{l'-l} \varphi_{\alpha\beta}(l\kappa; l'\kappa') \exp -i\boldsymbol{q} \cdot [\boldsymbol{r}(l\kappa) - \boldsymbol{r}(l'\kappa)]$$

where κ, κ' represent any of the n ions in the unit cell, M_κ and $M_{\kappa'}$ their mass and

$\varphi_{\alpha\beta}(l\kappa; l'\kappa')$ the force constants between ions κ and κ' belonging to cells l and l' (α, β represent the components of displacements of each ion in the three directions). In the rigid-ion model the potential φ is composed of two parts: (i) The so-called long-range interaction potential corresponding to electric interactions φ^c and giving rise to the Coulomb part of the dynamical matrix $\mathbf{C}^c(\boldsymbol{q})$ which can be calculated using standard programmes. In addition to the crystallographic parameters, this part depends only on the effective ionic charge. In the case of tetrafluoroaluminates, only three parameters are involved: Z_{Al}, Z_{Rb}, $Z_{F_{eq}}$, the last one ($Z_{F_{ax}}$) being determined by the total electric neutrality. The opportunity of different effective charges for F_{ax} and F_{eq} is considered to be due to the large differences of the neighbourhood of these ions. (ii) The short-range interaction potential φ^r giving rise to the dynamical matrix $\mathbf{C}^r(\boldsymbol{q})$. In the ideal structure of the $RbAlF_4$ there are seven different interactions between nearest neighbours: Al–F_{eq}, Al–F_{ax}, Rb–F_{ax}, Rb–F_{cq}, F_{ax}–F_{ax}, F_{ax}–F_{eq} and F_{eq}–F_{eq}. In the usual approximation where the potential energy of the crystal is the sum of a pair of ions interactions the tensors are symmetrical. Moreover the ions considered here have spherical symmetry and the potentials are axially symmetric. Thus the interaction between two ions can be characterised by two parameters A_i and B_i such that

$$A_i = \frac{2V}{e^2}\left(\frac{\partial^2 U_i(\boldsymbol{r}_i)}{\partial r_{i\parallel}^2}\right)_0 \qquad B_i = \frac{2V}{e^2}\left(\frac{\partial^2 U_i(\boldsymbol{r}_i)}{\partial r_{i\perp}^2}\right)_0$$

where $U_i(\boldsymbol{r}_i)$ represents the potential energy of pairs and $\Gamma_{i\parallel}$ and $r_{i\perp}$ the displacements parallel and perpendicular to the ionic bond, respectively (V is the volume of the unit cell and e the electron charge). The subscript 0 means that the derivatives are taken at equilibrium.

Since each kind of interaction can be characterised only by the two parameters A_i and B_i, in the ideal phase of $RbAlF_4$ only 14 parameters are involved. Assuming central interactions A_i and B_i are given by:

$$A_i = \frac{2V}{e^2}\left(\frac{\partial^2 U_i(r_i)}{\partial r_i^2}\right)_0 \qquad B_i = \frac{2V}{e^2}\frac{1}{r_{i0}}\left(\frac{\partial U_i(r_i)}{\partial r_i}\right)_0$$

(r_{i0} is the equilibrium distance) and assuming a Born–Mayer potential:

$$U_i(r_i) = \lambda_i \exp - (r_i/\rho_i)$$

they are connected through the relation

$$A_i/B_i = - r_{i0}/\rho_i$$

where ρ_i characterises the distance of interaction. This relation can again reduce the number of parameters.

Finally, the rigid-ion model for the AMF_4 involves less than 14 short-range interaction parameters plus three effective charges, giving less than 17 independent parameters.

4.2. Parameters to be refined

The long- and short-range interactions also depend on the lattice and structure parameters. We have calculated the phonon spectrum at 400 °C where, according to Bulou and Nouet (1982), the parameters are:

$$a = b = 3.659\ \text{Å} \qquad c = 6.306\ \text{Å} \qquad z = 0.277$$

Table 4. Interionic distances in $RbAlF_4$ and range of variations of the rigid-ion model parameters giving a discrepancy less than 20% between experimental and calculated frequencies. The last column gives the values adopted to calculate the phonon spectrum represented in figure 6 and in table 6, which corresponds to a discrepancy of less than 10% between calculated and experimental frequencies.

Interaction parameters	Interaction	Distances	$A_i \cdot B_i$	Range	Adopted solution
Short range	Al–F_{eq}	1.830	A_1	110–160	155
			B_1	−11.6–−18	−15.5
	Al–F_{ax}	1.747	A_2	208–246	224
			B_2	−18–−24	−22.4
	Rb–F_{eq}	3.645	A_3	0.94–1.40	1.06
	Rb–F_{ax}	2.945	A_4	10.4–13	10.8
	F_{eq}–F_{eq}	2.587	A_5	13.4–22	15.92
	F_{eq}–F_{ax}	2.529	A_6	20.6–28.6	21.88
	F_{ax}–F_{ax}	2.812	A_7	3.4–5.2	4.6
Long range			Z_{Al}	1.9–2.3	2.19
			Z_{Rb}	0.80–1.00	0.84
			Z_F	−0.73–−0.82	−0.7575

The distances between ions can be deduced from these parameters, as reported in table 4. These parameters are experimental data that do not have to be adjusted.

As shown above, 17 parameters are to be refined. However in the study of lattice dynamics of alkaline halogenides the A_i/B_i ratio for A–F interactions has been found close to −10. Such a ratio has been used also for the A–F and F–F interactions in the description of the phonon spectrum of fluoroperovskites AMF_3 and they give convenient results (Rousseau *et al* 1977). Although, according to table 4, the interionic distances in $RbAlF_4$ are somewhat different, the relative variation is small, and in the framework of a Born–Mayer potential they remain in the same range. Thus in the rigid-ion model of $RbAlF_4$ a further reduction in the number of parameters to be refined is obtained by setting A_i/B_i equal to −10 for the rubidium–fluorine and fluorine–fluorine interactions.

4.3. Experimental data

The experimental data used to determine the model parameter values are the acoustic velocities, the M_3, M_6, M_9^1, X_7^1 and X_3^1 mode frequencies (determined at 400 °C by inelastic neutron scattering) and the Γ_1, Γ_9, M_9^2 and X_3^2 mode frequencies determined by Raman scattering (Bulou *et al* 1983). The values of these frequencies and the sound velocities modes are given in table 5. As can be seen, the M_9^2 and X_3^2 mode frequencies have been measured respectively in phases II (at 293 K) and III (at 20 K); it is reasonable to think that the frequencies of such modes are quite temperature-independent.

4.4. Refinement

In order to reduce the computing time, the determination of the Z_i, A_i and B_i parameters was performed in two steps: in the first step using analytical expression of several frequencies the magnitude of the parameters was determined to obtain a difference between the other experimental and calculated values less than 20%. The second

Table 5. Experimental and calculated (at 400 °C) mode frequencies and ultrasonic velocities in $RbAlF_4$. The experimental technique of investigation is indicated by R (Raman scattering study) or n (inelastic neutron scattering study). I, II and III refer to the phase in which the measurements were performed. The last column gives the difference (in %) between experimental and calculated values. The model parameters are reported in table 4.

Phonon	Measurement technique	$\omega_{exp}(cm^{-1})$	$\omega_{calc}(cm^{-1})$	Discrepancy (%)
Γ_1	$R(I - A_{ig})$	538	513	4.6
Γ_9	$R(I - E_g)$	235	214	8.9
M_3	n(I)	13	14	7.7
M_6	n(I)	63	63	0
M_8^1	n(I)	43	46	7.0
M_9^2	$R(II - E_g)$	354	375	5.9
X_5^1	n(I)	18.3	20	9.3
X_5^2	$R(III - A_g)$	93	85	8.6
X_7^1	n(I)	60	63	5.0

q direction	$e/\|e\|$	Symmetry	Measurement technique	$v_{exp}(m\ s^{-1})$	$v_{calc}(m\ s^{-1})$	Discrepancy (%)
110	110	Σ_1	n(I)	4913(80)	4774	2.8
	$1\bar{1}0$	Σ_3	n(I)	3493(130)	3547	1.5
	001	Σ_4	n(I)	2122(50)	2158	1.7
010	010	Δ_1	n(I)	5204(150)	5730	9.2
	100	Δ_4	n(I)	2892(40)	2800	3.2
	001	Δ_3	n(I)	2267(40)	2228	1.7
001	001	Λ_1	n(I)	4569(30)	4994	9.3
	100	Λ_5	n(I)	2166(30)	2005	7.4

step corresponded to the refinement of the parameters; the difference between all experimental and calculated frequencies is less than 10%.

While no data has been published on Al–F interactions, the values of the Rb–F and F–F interactions can be estimated from previous studies of the dynamical properties of MgF_2 (Almairac and Benoît 1974) and $RbCaF_3$ (Rousseau *et al* 1977) in which the interionic distances are close to those encountered in $RbAlF_4$. Moreover, among the modes chosen to determine the parameters of the model, the Γ_1, Γ_9, M_3 and M_6 symmetry modes appear only once and so an analytical expression of their frequency can be obtained. As an example, the analytical expression of the M_3 mode frequency is given in § 5. They permit analytical expressions of four parameters which reduce the computing time: the Γ_1, Γ_9, M_3 and M_6 mode frequencies are mainly driven by parameters A_2 (about 70%), A_6 (about 90%), B_1 (about 70%) and A_4 (about 70%), respectively. The range of parameters so determined, such that discrepancies between experimental and calculated values are less than 20%, is given in table 4. The results are consistent with the values expected from studies of MgF_2 and $RbCaF_3$. It appears that the ratio A_i/B_i for the Al–F interaction is close to -10, as for the other interactions. The effective charges lie in a wide range: 1.9 to 2.3 for Al, 0.80 to 1 for Rb and -0.73 to -0.82 for F.

From the first step some experimental frequencies (Γ_1, Γ_9, M_3, M_9) are exactly the

experimental frequencies since they are introduced in the analytical expression of some constants; on the other hand, a discrepancy of up to 20% can appear for other frequencies. In order to obtain a confident description we search in the range of the parameters determined in the first step all the sets of parameters reducing the total discrepancy between experimental and calculated frequencies and a discrepancy of less than 10% has been obtained (table 5). In light of the first step results the same charge has been attributed to the F_{ax} and F_{eq} fluorines and the ratio A_i/B_i has been set to -10 for all interactions. This reduces to only nine the total number of parameters required to describe the phonon spectrum of $RbAlF_4$.

In the search for solutions 'at 10%' it appears that the short-range forces lie in a narrow range. On the other hand, the set of effective charges is very large and the number of solutions, consistent with experimental frequencies, remains large. The

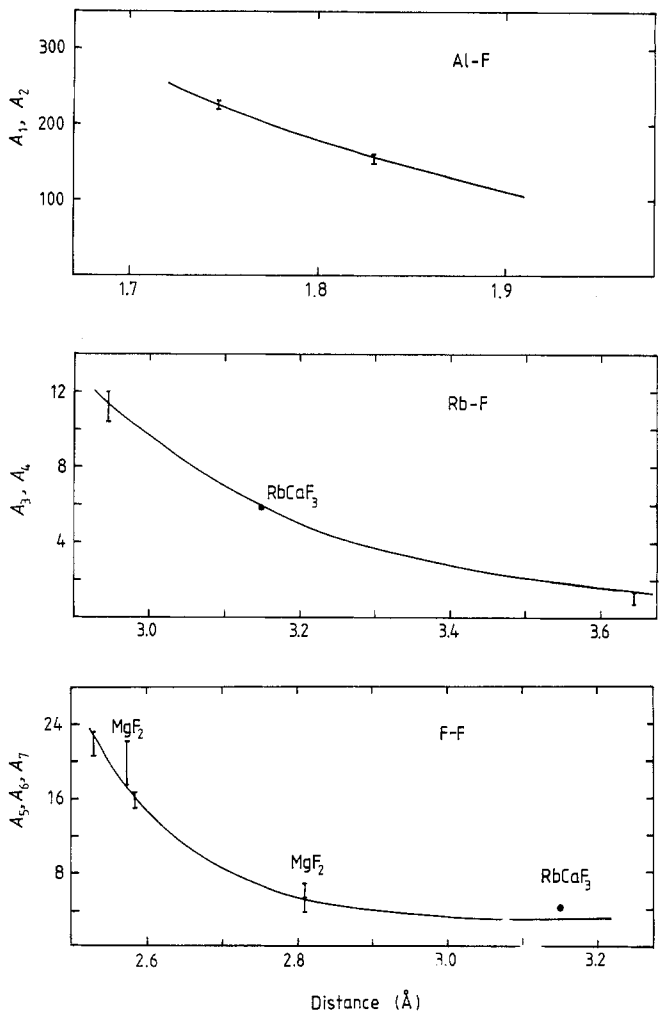

Figure 9. Short-range interaction parameters A_i versus interionic distances as refined in $RbAlF_4$. Comparison with data available on $RbCaF_3$ and MgF_2 (with respect to $RbAlF_4$ cell volume).

phonon spectrum has been calculated for different sets of parameters including in particular the cases of effective charges close to and far from the nominal charges. In all cases similar phonon spectra have been obtained. The solution chosen is pesented in table 4.

The values of the force constants describing the phonon spectrum 'at 10%' are plotted in figure 9. These values agree fairly well with previous results deduced from $RbCaF_3$ and MgF_2 lattice dynamics studies. In particular, the interionic distance dependence of the Rb–F interaction can be described by a Born–Mayer law $A = \alpha \exp(-r/\rho)$, where $\rho = 0.301$ (full line of figure 9), a value in good agreement with that obtained for RbF studies. The F–F interactions are also in agreement with the values obtained for MgF_2. The full line of figure 9 corresponds to a Born–Mayer interaction with $\rho = 0.20$. In figure 9 Al–F interactions against distance are also reported; to our knowledge no data have been published on such kinds of interaction. Note that the values are in agreement with the hypothesis used for the fit of the spectrum, that is, in the framework of a Born–Mayer potential, according to A_1 and A_2 we found $\rho = 0.20$ and so the ratio $A_i/B_i = -r/\rho = -9$, close to the ratio -10. It can also be noted that these values are very close to those obtained for the interaction of fluorine with divalent cation in $RbCaF_3$ or MgF_2, where the interionic distances are larger.

5. Discussion of the phonon spectrum of $RbAlF_4$

In table 5 are reported the experimental and calculated phonon frequencies and ultrasonic velocities corresponding to the parameters of table 4. The good agreement between experimental and calculated values (discrepancies less than 10%) can also be seen from the plot of the low-frequency phonon spectrum presented in figures 6(*a*) and (*b*).

It can be noted that according to macroscopic symmetry a common ultrasonic velocity may correspond to different set of wavevectors and polarisations (Launay *et al* 1983). However such coincidence is not always required by the symmetry of the dynamical matrix alone; it is satisfied only when every nucleus is in equilibrium and when the system is free of stress. It can be thought that our results satisfy the above conditions since, according to table 5 the sound velocities corresponding to Σ_4, Δ_3 and Λ_5 modes, which would be the same according to the macroscopic symmetry, stand in a narrow range (2158, 2228 and 2005 m s^{-1}, respectively).

Table 6 gives the calculated frequencies of modes corresponding to the high-symmetry points Γ, M, X, Z, A and R, and in figures 6 the calculated low-frequency phonon spectra are presented.

5.1. Main features of the spectra

The first use of the calculation of the phonon spectrum concerns the experimental investigation by inelastic neutron scattering: in addition to an *ab initio* estimation of the phonon dispersion curves it enables the dynamical structure factor to be calculated in order to optimise the time of investigations.

Figure 6 indicates the atomic displacements corresponding to the different phonons at the high-symmetry points. It can be seen that all the low-frequency modes can be attributed either to AlF_6 octahedral rotations (M_3, M_9^1, R_3^1, A_3) or to translations of Rb ions (M_6, M_{10}^1, X_7^1, X_1^1, R_2, R_6, R_8, Z_9^1, Z_1^1, A_7^1) or to combination of these motions

Table 6. Calculated phonon frequencies (in cm^{-1}) of $RbAlF_4$ at 400 °C for the six high-symmetry points of the tetragonal primitive Brillouin zone. The model parameters are given in table 4.

	Γ_4^i				Γ_{10}^i	
Γ_1	TO	LO	Γ_8	Γ_9	TO	LO
513	98	142	260	214	86	103
	468	476			206	213
	660	772			381	478
					594	665

X_1^i	X_3^i	X_4^i	X_5	X_6^i	X_7^i	X_8^i
107	20	117	212	231	63	137
446	85	321		268	256	386
591	385	591		605		639

Z_1^i	Z_4^i	Z_8	Z_9^i	Z_{10}^i
102	120	260	62	46
496	484		226	200
	776			379
				594

M_1^i	M_3	M_4^i	M_5	M_6	M_7	M_9^i	M_{10}^i
438	14	257	453	63	402	46	89
647		631				375	240
							500

A_1^i	A_3	A_4^i	A_5	A_7^i	A_9^i	A_{10}^i
407	14	278	453	63	65	221
644		649		402	102	496
					383	

R_1^i	R_2	R_3^i	R_4^i	R_5	R_6^i	R_7	R_8^i
414	63	93	106	222	67	256	98
586		402	318		213		393
			591		260		665
					589		

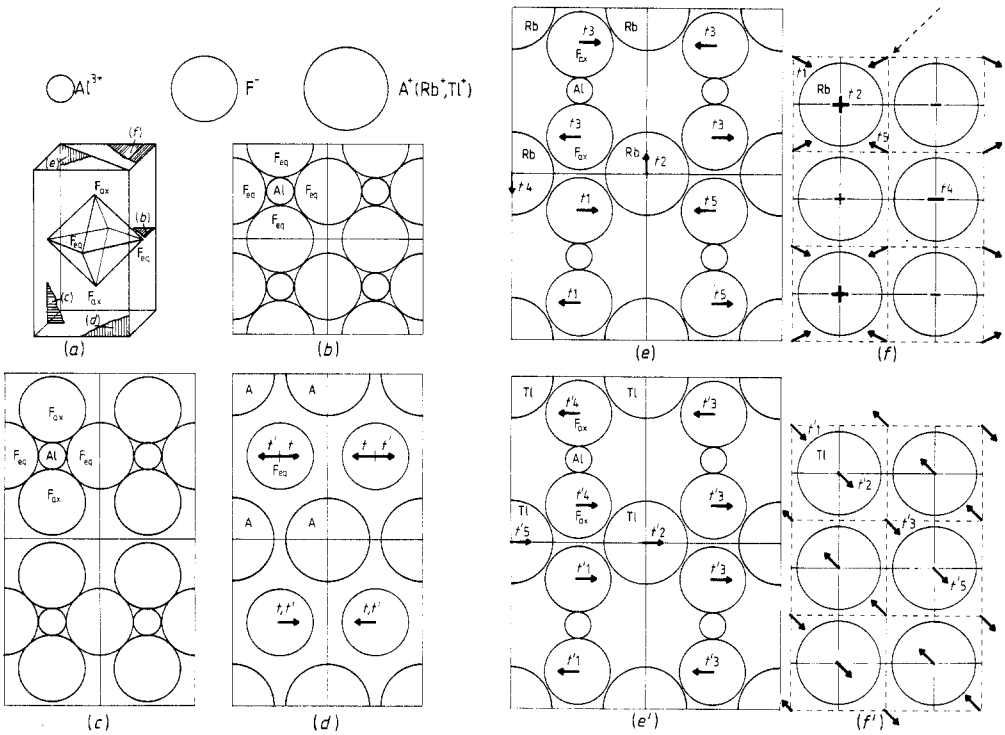

Figure 10. Selected sections of tetrafluoroaluminates $RbAlF_4$ and $TlAlF_4$ in their ideal high-temperature phase (*a*). The different sections are represented in (*b*)–(*e*) (four cells) and (*f*) (six cells). Full lines represent the unit cell sides; ionic radii and cell parameters are drawn to scale. (*b*) (001) plane showing equatorial fluorines. (*c*) (100) plane containing octahedra. (*d*) (100) plane containing A^+ and equatorial fluorines; Arrows indicate the F_{eq} displacements due to AlF_6 octahedra tilts around the |001| axis in $RbAlF_4$(*t*) and $TlAlF_4$(*t'*). (*e*, *e'*) Diagonal (110) planes showing the mechanism of ion displacements in $RbAlF_4$ (*e*) and $TlAlF_4$ (*e'*). (*f*, *f'*) (001) plane containing A^+ ions in $RbAlF_4$ (*f*) and $TlAlF_4$ (*f'*). The arrows starting from the intersection of dashed lines represent the displacements of axial fluorines located in a plane below the A^+ sheet. The amplitude of displacement of A^+ ions is proportional to the size of the + and − above and below the sheet, respectively.

(X_3^1, X_3^2, A_9^1, A_9^2). This result proves the rigidity of the octahedra since distortion vibrations lie in a higher frequency range. In fact, it corroborates the results obtained from a sterical analysis of the structure: if we draw to scale the ions (ionic radii given by Shannon 1976) in a unit cell (figure 10) it appears that the AlF_6 octahedra are probably the more compact and rigid MF_6 octahedra (figures 10(*b*), (*c*)) since Al^{3+} (the smallest trivalent ion) just fills the free space at centre of a close packet F_6 octahedron. In figure 10(*b*) and (*d*) it can also be seen that octahedra can easily rotate around the tetragonal axes without any Rb displacement.

According to figure 6 the lower-frequency modes are the M_3 mode (AlF_6 tilt around [001]) and X_3^1 mode (AlF_6 tilt around [100] and [010] plus Rb translation along [001]), i.e., the modes which condense at 280 °C and 9 °C, respectively. Note that the frequency of the modes setting between M_3 and A_3 (V_2 branch) is constant (or variation less than

0.1 cm^{-1}) and is given by:

$$\omega^2 = (e^2/VM_F)[B_1 + 2(A_3 \cos^2\vartheta + B_3 \sin^2\vartheta) + 2B_5 + 2B_6 - Z_{F_{eq}}(18.253\, Z_{Al} - 1.378\, Z_{Rb} + 2.838\, Z_{F_{eq}} + 8.724\, Z_{F_{ax}})].$$

The low frequency of such modes results from the competition between positive Coulomb interactions and negative short-range interaction. All these phonons correspond to rotations around [001], either in phase (at the M point) or in opposite phase (at the A point); this result recalls the property of the quasi-flat RM branch in perovskites between R_{25} and M_3 modes (Rousseau *et al* 1977). While the two-dimensional correlations are easily explained by the gearing of rigid octahedra the three-dimensional correlations cannot be explained; the phonon spectrum of $RbAlF_4$ does not explain why the transition at T_{C1} results from condensation at the M point rather than at the A point.

Note that sterical arguments also enable the low frequency of the X_3^1 mode and the three dimensional correlations to be explained. Let us consider figure 10(*e*) and (*f*). It can be seen that the AlF_6 octahedra rotations around [100] axis are favoured by the Rb displacements along the [001] axis which, in addition, explain the sense of the octahedra tilts in the neighbouring AlF_6 sheets. (An alternative solution can be obtained by A^+ displacement parallel to the octahedral planes: the corresponding transition in $TlAlF_4$ is presented for comparison in figures 10(*e'*) and (*f'*). Then, in contrast with perovskite, in $RbAlF_4$ the monovalent cations (Rb^+) seems to play a major role in the onset of the three-dimensional correlation of AlF_6 octahedra tilts. Indeed, in $KAlF_4$ where K^+ is smaller the X_3^1–M_0^1 line is flat and the three-dimensional correlations cannot be established (Bulou *et al* 1988).

Finally, the dispersion curves along the ΓZ line are consistent with the highly two-dimensional character of the material. The phonon spectrum in this direction has the well known aspect of a chain with two kinds of atoms (here two kinds of planes) for the

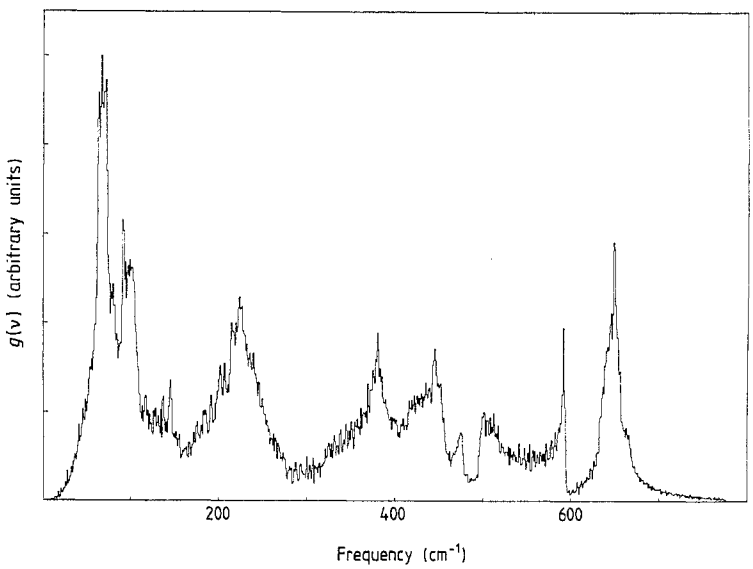

Figure 11. The calculated one-phonon density of states of $RbAlF_4$.

transverse modes (Λ_5^1, Λ_5^2) and the longitudinal modes (Λ_1^1, Λ_1^2) as well. The Z_{10}^1 and Z_9^1 correspond to pure translation modes of the octahedral sheets and the Rb sheets respectively (also for Z_1 and Z_4). This 'two-dimensional-like behaviour' is also expressed by the quasi-flat dispersion curves between M and A and between X and R.

5.2. *One-phonon density of states and anisotropic temperature factors*

Solving the dynamical matrix in 9828 independent $\boldsymbol{q}$ vectors forming a uniform mesh over 1/16 irreducible section of the first Brillouin zone, we have calculated the density of states as a function of phonon energy. The result is shown in figure 11. The more important feature is the presence of a sharp peak in the vicinity of 60 cm^{-1}, which is of particular importance in the analysis of Raman scattering results (see below).

5.3. *Discussion of Raman scattering results*

5.3.1. Identification of the B_{1g}, B_{2g} and B_{3g} modes. It is possible to estimate the validity of the calculated phonon spectra by checking that the frequencies are consistent with the experimental ones determined by Raman spectrometry in phase III, corresponding to B_{1g}, B_{2g} and B_{3g} symmetry phonons reported in table 7. Only one mode B_{1g} is observed with a frequency of 443 cm^{-1}. According to the compatibility relations diagram, such a mode comes from one of the four zone boundary modes of the ideal phase M_1^1, M_1^2, M_5 or X_5; as shown in table 6 the calculated frequencies are 438 cm^{-1}, 647 cm^{-1}, 453 cm^{-1}

Table 7. Experimental Raman scattering frequencies of $RbAlF_4$ (taken from Bulou *et al* 1983). For phases II and III the underlined values correspond to Raman lines not observed in phases I and II, respectively. In parentheses are given the corresponding symmetries in the ideal phase Brillouin zone whenever the attribution is unambiguous. In phase III, the B_{2g} and B_{3g} modes cannot be distinguished due to the domain structure. However, as can be seen from figure 5 to each B_{2g} mode corresponds a B_{3g} mode with the same frequency since these modes come from the splitting of a twice degenerated mode in phase II.

Phase I (730 K)

$1\,A_{1g}$	$1\,E_g$
538 (Γ_1)	235 (Γ_9)

Phase II (293 K)

$2\,A_{1g}$	$3\,E_g$	$1\,B_{1g}$	$1\,B_{2g}$
541 (Γ_1)	238 (Γ_9)		
<u>108</u> (M_3)	<u>354</u> (M_9)		

Phase III (20 K)

$9\,A_g$	$5\,B_{1g}$	$8\,(B_{2g} + B_{3g})$
543 (Γ_1)	<u>443</u>	238 (Γ_9)
129 (M_3)		355 (M_9)
<u>28.5</u> <u>44.5</u> (X^1_{00343})		<u>251</u>
<u>91</u> <u>95</u> (X^2_{00343})		<u>461</u>

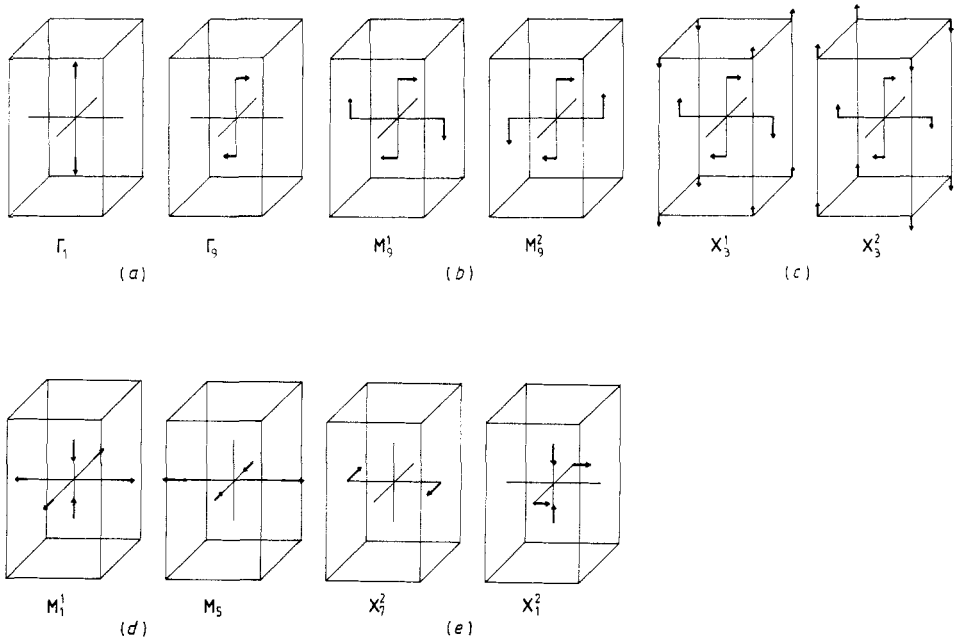

Figure 12. Approximate symmetry coordinates of the Raman active modes.

and 212 cm^{-1} respectively†. Then the frequency measured at 443 cm^{-1} can be attributed to the M_1^1 or M_5 modes. The atomic displacements corresponding to these modes are shown in figure 12(*d*).

The frequencies of the B_{2g} and B_{3g} modes specific to phase III are at 251 cm^{-1} and 461 cm^{-1} (table 7). According to the affiliation diagram these modes arise from the X_1 and X_7 modes (since the Γ_9 and M_9^i are already attributed). According to table 6 the calculated frequencies‡ of these modes are

$$X_1^1 = 107\ cm^{-1} \qquad X_1^2 = 446\ cm^{-1} \qquad X_1^3 = 591\ cm^{-1}$$

$$X_7^1 = 63\ cm^{-1} \qquad X_7^2 = 256\ cm^{-1}.$$

Thus the experimental frequencies at 461 cm^{-1} and 251 cm^{-1} can be attributed to the X_1^2 and X_7^2 modes, respectively (the X_7^1 frequency is known from the inelastic neutron scattering studies); the atomic displacements corresponding to these modes are presented in figure 12(*e*). The model results are consistent with the experimental data obtained by Raman spectrometry in phase III of $RbAlF_4$.

5.3.2. Interpretation of the Raman anomalies. The calculated phonon frequencies enable one to estimate the frequency of the Raman-active modes not observed, such as the M_9^1 mode. Using the calculated characteristic of this phonon (frequency and dynamical

† The M_5 and X_5 mode frequencies can be calculated with a simple analytical expression. In the search for the model parameters their frequency ranges have been determined.

‡The X_7^2 frequency has been calculated from the different sets of parameters and it ranges from 240 cm^{-1} to 275 cm^{-1}.

structure factor) it has been located by inelastic neutron scattering at 43 cm^{-1} at 400 °C and in the same frequency range at room temperature. It is an octahedral tilt mode (figure 12(*b*)). The second M_9 mode (M_9^2) is an octahedral distortion mode (figure 12(*b*)) with a frequency of 354 cm^{-1}, as measured by Raman scattering.

Although the M_9^1 mode is not observed by Raman spectrometry in the expected configuration, the Raman spectrum exhibits in the same frequency range a large and asymmetric line that softens when T_{c2} is approached (Bulou *et al* 1983). This soft behaviour suggests that this feature can be attributed to phonons close to X_3^1, which condenses at T_{c2} (Y_2 or W_3) or to the M_9^1 mode itself, although the experimental configuration of observation does not correspond to such a symmetry.

The Raman scattering spectra of $RbAlF_4$ also present an unexpected large line in the vicinity of 120 cm^{-1}. According to the calculated phonon spectrum no singularity can be predicted in such a frequency range and all attempts to confirm the existence of a mode in this frequency range by inelastic neutron scattering have failed. On the other hand, such a frequency is about twice the frequency of the flat phonon branch $X_7^1W_2^1R_2U_2^1Z_9^1$ (Rb translatory modes along [100] and [010]) or along $A_7^1V_3M_6$ (Rb translatory modes along [001]) responsible for a sharp peak in the density of states (figure 11). At 673 K the frequencies of X_7^1 and M_6 modes measured by inelastic neutron scattering, are 60 cm^{-1} and 63 cm^{-1}, respectively. Then the 'forbidden' Raman line in the vicinity of 120 cm^{-1} could be imputed to a two-phonons Raman scattering process. According to the experimental condition of observation (ZZ) it could be imputed to Rb^+ translation along [001] (V_3 branch). The important intensity of the line can be attributed to the fact that, in addition to the flat character of the V_2 branch, such modes involve Rb^+ displacements which, in $RbAlF_4$, are the more efficient ions for light-scattering processes. Note also that such an explanation is also in agreement with the frequency position of the forbidden lines also observed in $KAlF_4$ and $TlAlF_4$ (in preparation).

5.3.3. Reinvestigation of the infrared absorption results. The infrared absorption spectrum of $RbAlF_4$ collected at room temperature has been published by Soga *et al* (1974). According to the compatibility relations diagram seven and ten lines are infrared-active in phases I and II, respectively, with the following symmetries:

phase I (D_{4h}^1) $\quad 3A_{2u} \oplus 4E_u$

phase II (D_{4h}^5) $\quad 3A_{2u} \oplus 7E_u$

When Soga *et al* performed their IR study it was thought that at room temperature $RbAlF_4$ had the ideal structure and they searched for seven lines. The experimental frequencies measured by Soga are reported in table 8, together with the attribution proposed by the authors on the basis of a valence force field.

The frequency measured by IR absorption spectrometry roughly corresponds to the frequency of the transverse optic mode. We can compare the results of our model at 400 °C (in phase I) to the experimental data of Soga *et al* (at room temperature). The attribution is facilitated by presenting the experimental and calculated results on a diagram such as figure 13. This attribution is established by taking into account the dispersion of the calculated values as determined for various sets of model parameters: this range of variation is indicated in figure 13.

Concerning the low-frequency phonon spectrum, the 94 cm^{-1} and 116 cm^{-1} frequencies are imputed to the Γ_{10}^1 and Γ_4^1 modes, respectively, since the Γ_4^1 frequency is

Table 8. Observed and calculated (using a valence force field) IR absorption frequencies (in cm^{-1}) in $RbAlF_4$ at room temperature (according to Soga *et al* 1974).

	$RbAlF_4$	
Species	Observed	Calculated
$A_{1g}\ \nu_1$		510
$E_g\ \nu_2$		185
$A_{2u}\ \nu_3$	585	585
$A_{2u}\ \nu_4$	116	117
$A_{2u}\ \nu_5$	243	243
$B_{2u}\ \nu_6$		216
$E_u\ \nu_7$	735	735
$E_u\ \nu_8$	94	93
$E_u\ \nu_9$	208	208
$E_u\ \nu_{10}$	341	341

always higher than Γ_{10}^1. These modes correspond to displacements of Rb^+ sheets with respect to the AlF_6 one (figure 14). This conclusion agrees with the analysis of Soga *et al*.

For the highest-frequency modes ($\Gamma_4^3, \Gamma_{10}^4$) it is observed from figure 13 that Γ_{10}^4 frequency is always less than that of Γ_4^3. Thus the 735 cm^{-1} and 585 cm^{-1} lines are

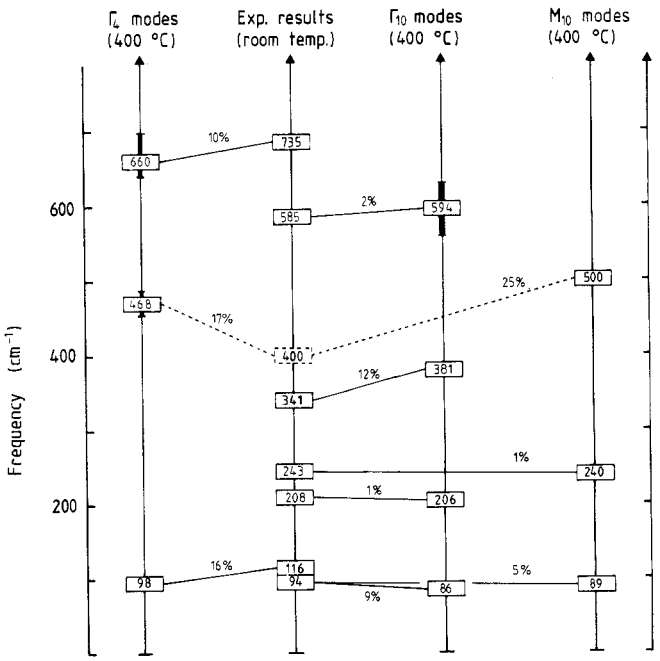

Figure 13. Identification diagram for attribution of the infrared active modes at room temperature in $RbAlF_4$. The calculated frequencies correspond to parameters given in table 4 (at 400 °C). Heavy lines correspond to the range of variation of the calculated frequencies for different sets of parameters.

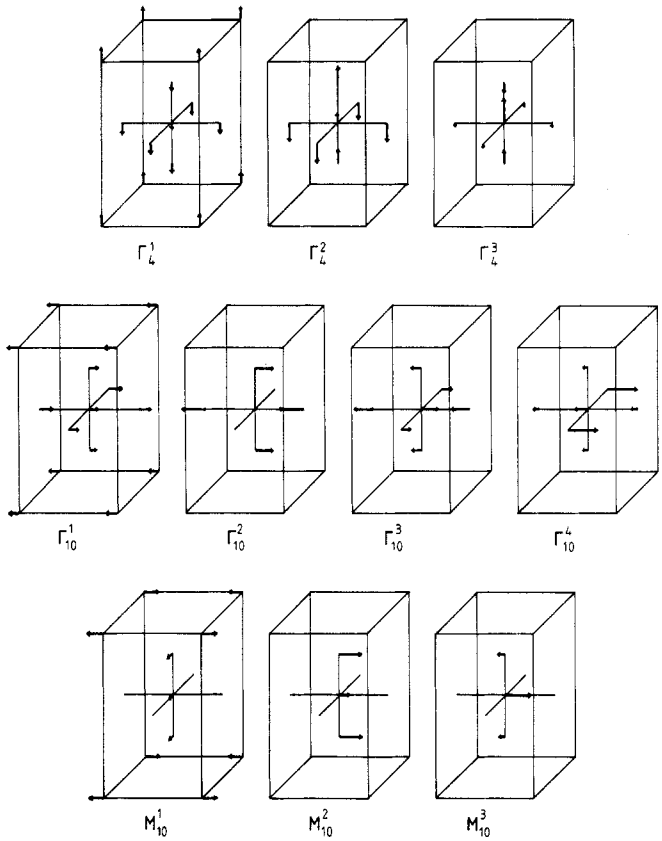

Figure 14. Approximate symmetry coordinates of the infrared absorption active modes (TO modes) in phase I (Γ modes) and phase II (Γ and M modes).

attributed to the Γ_4^3 and Γ_{10}^4 modes, respectively. The former corresponds to Al–F_{ax} stretching and the second to octahedral distortion (figure 14). The opposite attribution was proposed by Soga *et al.*

It can be thought that the 208 cm^{-1} corresponds to the Γ_{10}^2 mode (calculated value 206 cm^{-1}) and the 341 cm^{-1} corresponds to the Γ_{10}^3 mode (381 cm^{-1} calculated). On the other hand, according to our model the 243 cm^{-1} line cannot be attributed to one of the Γ_4 or Γ_{10} mode. However, it should be noted that the IR spectrum has been obtained at room temperature, i.e., in phase II when the M_{10} modes of phase I are IR-active (figure 5). Then the IR absorption line at 243 cm^{-1} could be attributed to the M_{10}^2 mode, calculated at 240 cm^{-1}. This line would disappear above T_{c1}. The ionic displacements corresponding to the M_{10} modes are presented in figure 14.

Note also that a line in the vicinity of 400 cm^{-1} is observed on the spectra collected by Soga *et al*, although the authors did not mention it. This line could be attributed to the Γ_4^2 mode (discrepancy between calculated and experimental values 17%); however, although the discrepancy is greater (25%) it is possible to attribute this line to the M_{10}^3 mode. Indeed, owing to the ionic displacements involved, it can be assumed that the M_{10}^3 mode frequency is lower in phase II than in phase I due to the 'relaxation' consecutive to the tilt around the [001] axis.

Then the attribution proposed according to our model is somewhat different from that of Soga *et al*. Though not used in the refinement, the measured IR frequencies can be identified to the calculated ones. Note also that in their model Soga *et al* found an Al–F_{ax} interaction smaller than the Al–F_{eq} one. From structural studies it is known (Bulou *et al* 1982) that the Al–F_{ax} distance is shorter than Al–F_{eq}, so that we would expect an Al–F_{ax} interaction greater than Al–F_{eq}, in agreement with the present results.

6. Conclusions

In this paper we have reported the first investigations of the phonon spectrum of the layered perovskite $RbAlF_4$ in its higher symmetry phase. The symmetries of the normal modes of vibration have been calculated at all symmetry points and symmetry lines of the tetragonal Brillouin zone and the ionic displacements have been presented.

From symmetry arguments it has been predicted that the two structural phase transitions of $RbAlF_4$ at $T_{c1} = 280$ °C and at $T_{c2} = 9$ °C, arising from AlF_6 octahedral rotations around the [001] axis at T_{c1} and [100] and [010] axes at T_{c2}, could be attributed to the condensation of the M_3 and X_3 symmetry modes, respectively. This result has been confirmed by inelastic neutron scattering investigations that showed that these modes have low frequency and that they soften when T_{c1} and T_{c2} are approached. This work corroborates the displacive character first evidenced by Raman spectrometry in the lower symmetry phases. The M_3 mode is much more overdamped than the X_3 mode and in both cases a zero-frequency component rises when the transitions are approached from above. These investigations also permit the low-frequency part of the phonon spectrum of $RbAlF_4$, to be measured, especially the frequency of a number of modes characteristic of the structure.

A programme based upon a rigid-ion model is written to describe the phonon spectrum of the layered AMF_4 materials in their ideal higher-symmetry phases. It involves only 10 parameters that have been adjusted (in case of $RbAlF_4$) according to inelastic neutron scattering results, ultrasonic velocities and Raman scattering frequencies, a total of 17 experimental data. The discrepancies between experimental and calculated data are less than 10%; the results are also consistent with IR spectroscopy frequencies, data that have not been used in the refinement. The results can be considered as reliable since they are based upon a large number of experimental data peculiarly owing to the existence of two structural phase transitions which 'bring' Brillouin zone boundary modes at the zone centre where they can be easily characterised by Raman scattering.

The first application of the model concerns the use of inelastic neutron scattering investigations via estimation of the phonon spectrum and calculation of the dynamical structure factor.

The dispersion curves of $RbAlF_4$ reveal that AlF_6 octahedra are very compact and rigid. They show that the low-frequency modes correspond either to AlF_6 octahedral tilt, either to Rb displacements alone or to the relative displacement of the AlF_6 network with respect to the Rb network. The structural phase transitions in this structure are probably related to such displacements. The frequency of a number of modes characteristic of the octahedral vibrations are given. Such data can be used in vibrational studies of more complex structures such as the β-structure of $RbAlF_4$ (Fourquet 1980), which undergoes a topotactic transition, or of amorphous materials and also for electronic studies of trivalent ions in octahedra (Ducouret-Cereze and Varret 1988).

On the basis of the calculated phonon spectra and the inelastic neutron scattering data it has been possible to explain the presence of the unexpected line observed in the Raman scattering spectra of $RbAlF_4$ in the vicinity of 120 cm^{-1}: this line is attributed to a two-phonon process corresponding to Rb vibrations along the [001] axis which contribute in the one-phonon density of states to a sharp peak in the vicinity of 60 cm^{-1}.

The short-range F–F interaction parameters behaviour against interionic distance is deduced from the model and the Al–F interaction is given for the first time; such data can be used for modelling the arrangement of amorphous AlF_3.

$RbAlF_4$, with the highest symmetry for the layered AMF_4 compounds, is the prototype of a wide variety of materials and its phonon spectrum can be considered as a reference. Since the dynamical model involves only a small number of parameters and since the interionic distance behaviour of the short-range interaction parameters are known for several pairs of ions it is possible to predict the phonon spectrum of compounds with a closely related structure. For example, it has been possible to predict which modes could be more probably involved in the phase transitions of $TlAlF_4$ and then predict the possible structures of the different phases (Bulou and Nouet 1987). Prediction of the phonon spectrum of $KAlF_4$ has enabled the mechanism of the martensitic transition in this material to be explained (Bulou *et al* 1989). The extension to investigate the properties of other AMF_4 compound is planned.

Acknowledgments

Greatest thanks are due to G Niesseron for technical assistance in crystal growth. The authors thank the LLB for neutron facilities and appreciate the CIRCE for computing efficiency.

References

Almairac R and Benoît C 1974 *J. Phys. C: Solid State Phys.* **7** 2614–29
Brosset C 1937 *Z. Anorg. Allg. Chem.* **235** 139–47
Bulou A, Gibaud A, Debièche M, Nouet J, Hennion B and Petitgrand D 1989 *Phase Transitions* **14** 47–53
Bulou A, Leblé A, Hewat A W and Fourquet J L 1982 *Mater. Res. Bull.* **17** 391–97
Bulou A and Nouet J 1982 *J. Phys. C: Solid State Phys.* **15** 183–96
—— 1987 *J. Phys. C: Solid State Phys.* **20** 2885–2900
Bulou A, Rousseau M, Nouet J, Loyzance P L, Mokhlisse R and Couzi M 1983 *J. Phys. C: Solid State Phys.* **16** 4527–37
Dagorn Y, Leblé A, Rousseau J J and Fayet J C 1985 *J. Phys. C: Solid State Phys.* **18** 383–95
Ducouret-Cereze A and Varret F 1988 *J. Physique* **49** 661–666
Fourquet J L, Plet F and De Pape R 1980 *Acta Crystallogr.* **B36** 1997–2000
Gibaud A, Bulou A, Launay C and Nouet J 1987 *J. Physique* **48** 625–33
Kovalev O V 1965 *Irreducible Representation of the Space Groups* (New York: Gordon and Breach)
Launay J M, Bulou A, Hewat A W, Gibaud A, Laval J Y and Nouet J 1985 *J. Physique* **46** 771–82
Launay J M, Bulou A and Nouet J 1983 *Revue Acoust.* **2** 61–4
Maradudin A A and Vosko S H 1968 *Rev. Mod. Phys.* **40** 1–37
Mockrin I and Kowalski A 1963 *US Patent Specification* 3098752
Rousseau M, Nouet J and Almairac R 1977 *J. Physique* **38** 1423–28
Rousseau M, Nouet J, Almairac R and Hennion B 1976 *J. Physique Lett.* **37** L33–5
Shannon R D 1976 *Acta Crystallogr.* **A32** 751
Shapiro S M, Axe J D, Shirane G, Riste T 1972 *Phys. Rev.* B **6** 4332
Soga T, Ohwada K and Iwasaki M 1974 *J. Chem. Phys.* **61** 1990–95
Warren J L 1968 *Rev. Mod. Phys.* **40** 38–76